EELS investigation of the electron conduction-band states in wurtzite AlN and oxygen-doped AlN(O)

V. Serin
Centre d'Elaboration de Matériaux et Etudes Structurales, Centre National de la Recherche Scientifique, Unité Propre de Recherche 8011, Boîte Postale 4347, 31055 Toulouse Cedex, France

C. Colliex
Laboratoire de Physique du Solide, Centre National de la Recherche Scientifique, Unité de Recherche Associée 002, Université Paris Sud, 91405 Orsay, France

R. Brydson
School of Process, Environmental and Materials Engineering, University of Leeds, Leeds LS2 9JT, United Kingdom

S. Matar
Institut de Chimie de la Matière Condensée de Bordeaux, Centre National de la Recherche Scientifique, Université Bordeaux 1, 33608 Pessac, France

F. Boucher
Institut des matériaux de Nantes, Centre National de la Recherche Scientifique, Boîte Postale 32229, 44322 Nantes, France

(Received 24 February 1998)

The electronic structures of pure and oxygen-doped AlN thin foils, grown by the chemical-vapor-deposition technique, have been thoroughly investigated using electron energy-loss measurements in a transmission electron microscope. This technique offers the advantage of providing spectral data with a typical sub-1-eV energy resolution from well-characterized areas. The interpretation of the experimentally determined electron energy-loss near edge requires the detailed comparison with theoretical calculations of unoccupied densities of states using self-consistent methods or from non-self-consistent multiple scattering calculations.
[S0163-1829(98)11131-1]

I. INTRODUCTION

The electronic structure of aluminum nitride (AlN) and that of its oxygen-doped derivatives [AlN(O)] are of great interest for several reasons, encompassing both fundamental as well as applied considerations. AlN is a ceramic with a bonding character that is more covalent than that found in the aluminum oxides and it possesses a large band gap of the order of 6.2 eV.[1] It exhibits excellent properties in terms of electrical resistivity, thermal conductivity, and mechanical strength, which make it particularly well suited to a wide range of engineering applications.[2–4] First, it is a very good candidate for tunable optoelectronic devices in the near vacuum ultraviolet range because it is easily alloyed with GaN, which crystallizes in the same wurtzite structure and offers a narrower band gap of 3.4 eV. Second, its high affinity for oxygen has stimulated its use as an oxidation-resistant coating.[5]

Among the techniques available for spectral investigation of electronic structure, electron energy-loss spectroscopy (EELS) performed with the high-energy electrons of a transmission electron microscope offers unique advantages: a good combination of energy resolution (down to about 0.7 eV) over a wide energy range (from about 1 to 2000 eV), and a spatial resolution (typically of the order of 1 to several nm), which makes it applicable to particular regions of the microstructure. In the case of aluminum nitride, EELS can be used to investigate the excitation of core electrons, on the anion through the study of the nitrogen K ionization edge at about 400 eV and on the cation through the Al L_{23} (at about 75 eV) and Al K (at about 1560 eV) edges. However, it must be emphasized that the information derived from the analysis of the fine structures occurring on these edges only concerns the distribution of the unoccupied electronic states. This makes this technique complementary to photoelectron or optical emission techniques, which predominantly probe the distribution of occupied states.

In order to extract full benefit from the EELS measurements, theoretical tools are required to model the observed distribution of electron states. These tools offer support for interpreting the origin of near-edge fine structures occurring under external treatments such as controlled oxygen doping. We can rely on recent theoretical developments for the calculation of electron densities of states (DOS) or for the description of the final states within the framework of multiple scattering schemes. The purpose of this paper is to combine a thorough EELS investigation of the relevant ionization edges in AlN and AlN(O) with the required density of states and multiple scattering calculations to elucidate both the atomic scale structure and electronic properties.

II. MATERIALS AND METHODS

Aluminum nitride samples were prepared by the chemical-vapor-deposition technique in a vertical hot-wall reactor using $AlCl_3$ and NH_3 as precursor gases and N_2 as

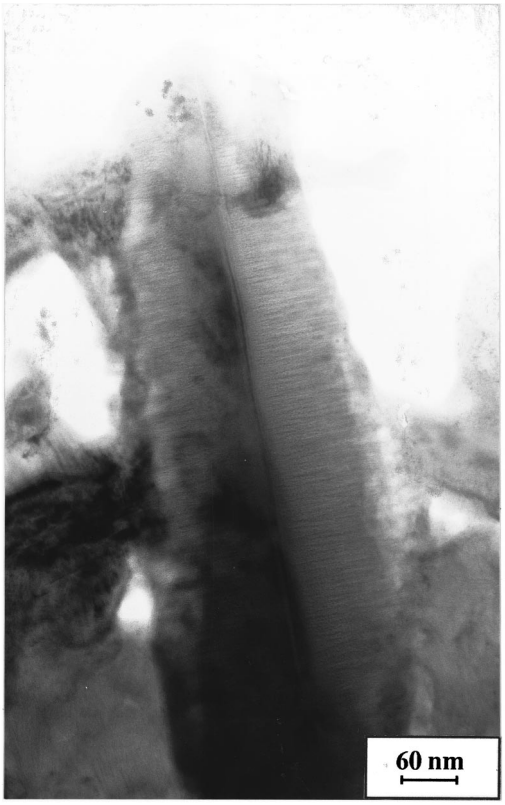

FIG. 1. TEM image of a dendritic crystal of O-doped AlN.

carrier gas. The influence of oxygen doping was studied by progressively increasing the N_2O partial pressure in the gas mixture. The total pressure in the reactor was 130 Pa and the temperature was about 1000 °C. The gross morphology of the deposited coatings on a Si substrate have been observed in a secondary-emission monitor by Aspar *et al.*[5] Thin foils for TEM observations were obtained by mechanical polishing followed by Ar^+-ion milling at liquid-nitrogen temperatures.

In the present work, we compare data obtained from a pure AlN polycrystalline deposit and from a deposit of oxygen-doped AlN grown under a ratio of partial pressures of N_2O and $AlCl_3$ equal to 15. In the former case (AlN), previous observations have shown a random distribution of crystals that are typically a few micrometers wide. In the latter case [AlN(O)], typical dendritic shapes are generally seen (see Fig. 1). They are made of an assembly of feather-like crystals. Each one consists of a core that is typically 20 or 30 nm wide and a few hundred nm long (the ''central part'') exhibiting on both sides a comb-shape pattern of contrast modulations (the ''external part'').

Electron energy-loss spectra were recorded using electron microscopes equipped with Gatan PEELS 666 (parallel energy loss spectrometers) operating under ELP (energy loss program). A Philips CM30ST operated at 100 kV was used; its high total current within a large probe makes it better adapted to the study of the Al *K* edge with a good signal-to-noise ratio. For advanced studies in terms of energy resolution (below 1 eV) and spatial resolution (below 1 nm) a VG HB 501 STEM (scanning transmission electron microscope) (operating at 100 kV) equipped with a field emission source was used, allowing discrimination between measurements on the central and on the external parts. However, this level of performance could only be obtained on the lower-energy edges, i.e., the Al L_{23}, the N *K*, and the O *K*, all lying well below 1 keV. This instrument, which is under full digital control, can also be used to monitor spectral changes occurring at regular time intervals or at regular steps of the probe across the specimen (special versions of the image-spectrum mode installed on this instrument[6,7]). Consequently data can be monitored either as a function of time (and dose) or of the precise location on the specimen, defined with a typical accuracy of 0.5 nm.

All EELS edges displayed hereafter have been processed for background subtraction, using a standard routine that models the preedge decay of the spectrum in terms of a power-law curve. The range of useful information above each edge extends over several tens of eV. It is common custom to distinguish, even if it may be rather arbitrary, several domains corresponding, respectively, to the threshold (about 10 eV wide maximum), to the near edge [also known as x-ray absorption near-edge structure (XANES) or ELNES (energy loss near edge structure) and covering up to about 50 eV] and to the extended region [also known as extended x-ray-absorption fine structure or EXELFS (extended energy loss fine structure) up to a few hundred eV]. In the present study, we will not consider the EXELFS, which has been thoroughly discussed in a previous paper.[8] Our purpose is to focus on the near-edge region. If the theory described below does not strictly discriminate threshold and XANES features, it may be important to emphasize that they suffer differently from the weight of multiple loss effects, due to the superposition of low-loss and core-loss events along the trajectory of the high-energy incident electron through the specimen thin foil. The most probable low-loss feature is the excitation of the bulk plasmon, which, in this type of specimen, lies between 20 and 25 eV. Consequently, multiple inelastic scattering predominantly modifies the core-edge fine structures in an energy domain starting only at energies about 15–20 eV above threshold. Consequently, for an analysis of fine structures over a wide energy range, i.e., up to about 60 or 80 eV above edges, a Fourier-ratio deconvolution procedure has been applied to remove multiple inelastic events. When the major concern of the study is restricted to the fine structures within a narrow window (less than 10 eV) above threshold, this procedure has been shown not to be required.

III. EELS RESULTS

A. Aluminum nitride

Figure 2 gathers our major results obtained from a pure aluminum nitride specimen. As a matter of fact, the EELS spectra often exhibit a weak O *K* signal that is mostly due to a surface oxide layer. Care has therefore been taken to select only spectra with a negligible oxygen contribution. The EELS spectra for Al *K*, N *K*, and Al L_{23} edges cover a range of 80 eV above threshold. In the last part of Fig. 2 we compare the details of the fine structures just above threshold recorded with the VG STEM: the two spectra have been aligned at the position of the inflection point, which by definition corresponds to the threshold energy. The different features are labeled $a-f$ and can be roughly gathered into two groups, a characteristic triplet 6 eV wide and a delayed maxi-

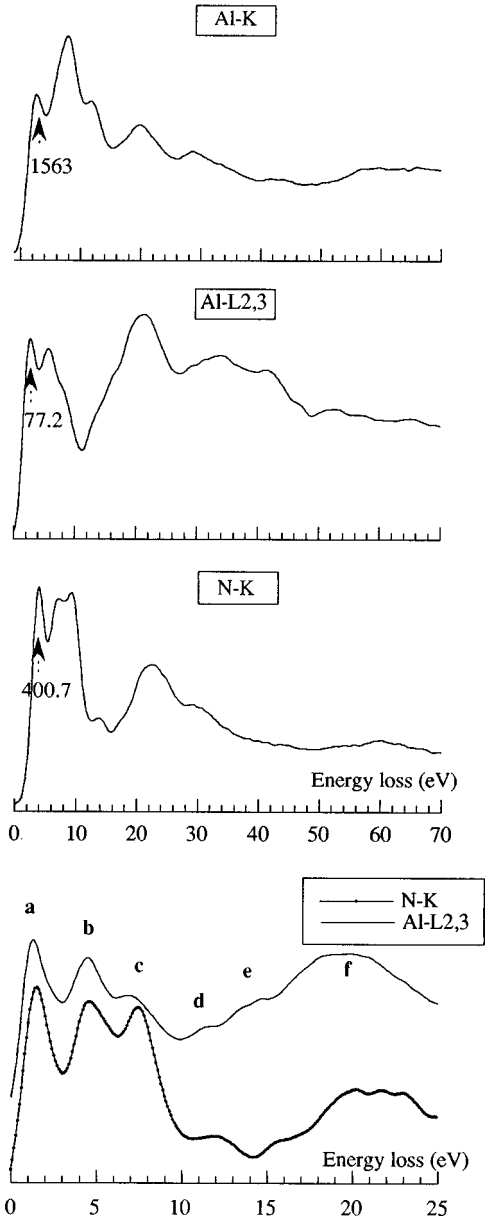

FIG. 2. Al *K*, Al L_{23}, and N *K* ELNES in pure AlN. In the last part of the figure the experimental results for N *K* and A L_{23} are shown with a higher energy resolution.

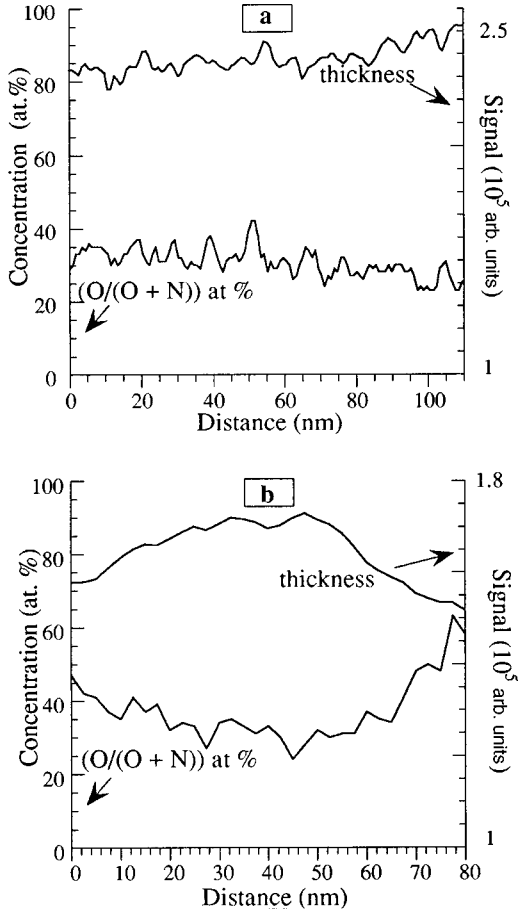

FIG. 3. Compositional profile issue from spectra obtained when scanning the incident probe (a) parallel with 1-nm steps, (b) perpendicular to the core of the dendritic crystal with 2.5-nm steps. Background substraction technique and normalization of both N *K* and O *K* signals with the relevant ionization cross section have been used.

mum *f* at about 20 eV above threshold. One can note a rather satisfying correspondence between the energy position of the six labeled features in both Al and N spectra. This triplet structure confined within a narrow range above threshold seems to constitute the rather characteristic aspect of the N *K* edge in aluminum nitride, when compared to different transition-metal mononitrides.[9]

B. Oxygen-doped aluminum nitride

The characteristic featherlike topography of the specimen requires spatially resolved elemental analysis. Using the line-spectrum mode we have measured the variation of both N *K* and O *K* signals (integrated over a 50-eV window following background subtraction) when scanning the probe perpendicular and parallel to the core of one of these dendrites. The corresponding results are gathered in Figs. 3(a) and 3(b), respectively. In each case we compare the total intensity within the measured energy loss range (from 350 to 650 eV encompassing the two characteristic edges), and the O/O+N ratio in atomic percent, taking into account the ratio of the relevant atomic cross sections. These curves relate the compositional changes to thickness changes: the thinner the specimen, the higher the oxygen proportion, with values ranging from about 20% in the center to 40% on the outer part of the dendrite. This variation may arise from differing bulk oxygen contents between the inner and the outer parts of the dendrite.[8] Along the direction parallel to the core the rather periodic fluctuations in the oxygen fluctuations seem to be in accordance with the contrast modulations visible in the TEM micrograph (Fig. 1).

Figure 4 shows a selection of fine structures recorded from local areas both on the core and on the outer part of the specimen. Compared to AlN, the N *K* ELNES from the central part exhibits a reduced intensity of the first peak, while in the outer part an opposite behavior of variable magnitude is observed. On the other hand, the changes visible on the Al edge on going from the center to the outer part of the dendrite are much less significant. Analogous comments also apply when comparing the shape of the O *K* edge on both parts of the AlN(O) feather: they are very similar. These

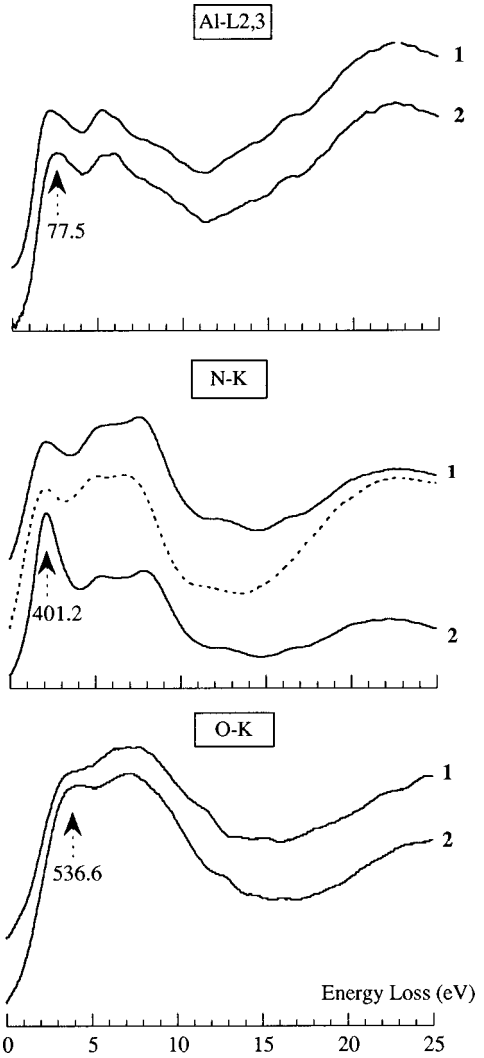

FIG. 4. Al L_{23}, N *K*, and O *K* ELNES in O-doped AlN (1, central part; 2, external part of the dendritic crystal). The N *K* shown in dotted lines has been recorded from the external part of the dendrite using a less intense probe (see text).

observations indicate that the nitrogen sites and environment are more affected by the doping.

The great diversity of behaviors observed at the N *K* edge, particularly intense when focusing the probe on the outer parts of the dendrite, suggests that this region is very beam sensitive. This effect should be particularly visible with the high current density probe in the dedicated STEM. As shown in Fig. 5, time-resolved sequences of spectra, recorded on a specimen with higher doping level, indicate the removal of oxygen, an increase in the absolute level of nitrogen and a spectacular rise of the first peak at threshold for the N *K* edge during irradiation.

IV. THEORETICAL FRAMEWORK

To interpret the above experimental results, which display a wide range of behaviors in terms of the general shape, number, and position of peaks in Al and N spectra, theoretical calculations are required. The ELNES results have therefore been modeled using the results of electronic structure calculations performed either from *ab initio* self-consistent

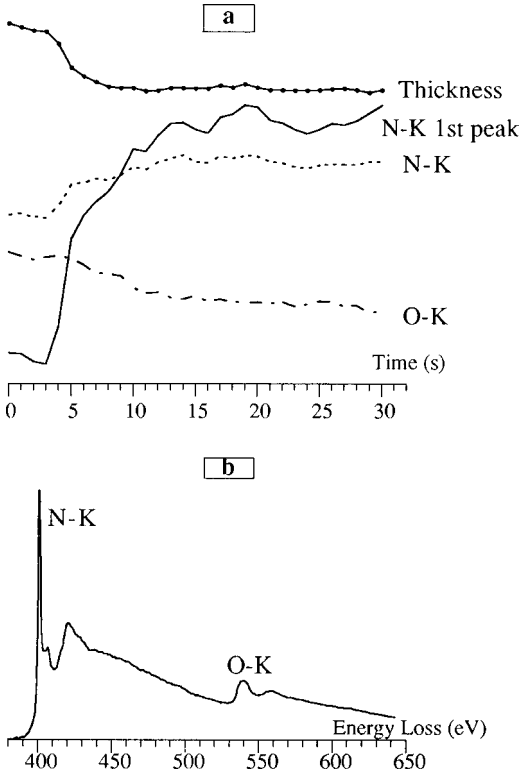

FIG. 5. (a) Evolution of the different signals measured during a time sequence of EELS spectra. The first five spectra correspond to a low flux of $\approx 10^6 e/\mathrm{nm}^2$ s while the following ones follow a brutal increase to a flux of $\approx 10^8 e/\mathrm{nm}^2$ s. The features measured in this sequence (N *K*, N *K* first peak, and O *K*) are shown in (b).

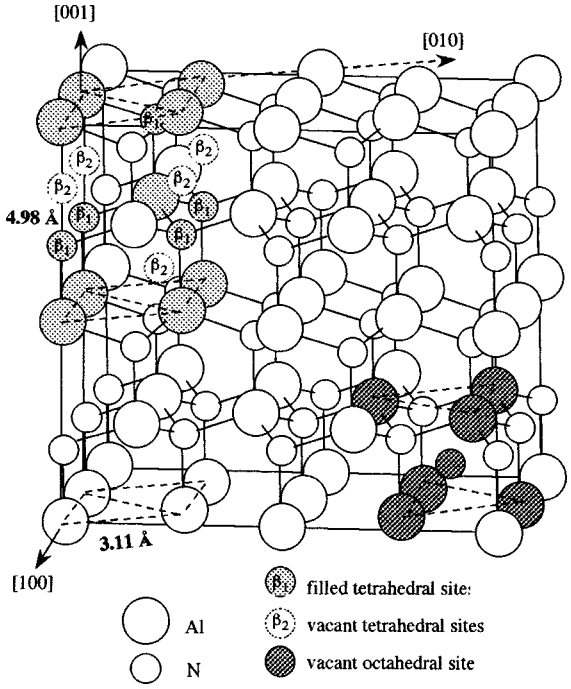

FIG. 6. Hexagonal structure of AlN. A unit cell is isolated in the upper side of the figure, while an octahedral site and its sixfold Al are highlighted in the lower side.

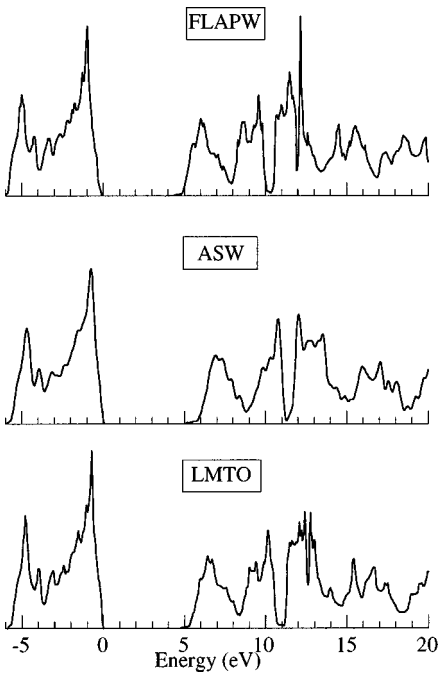

FIG. 7. Comparison of the total density of states (states/eV cell) using FLAPW (Ref. 24), ASW (Ref. 24), and LMTO (Ref. 25) methods.

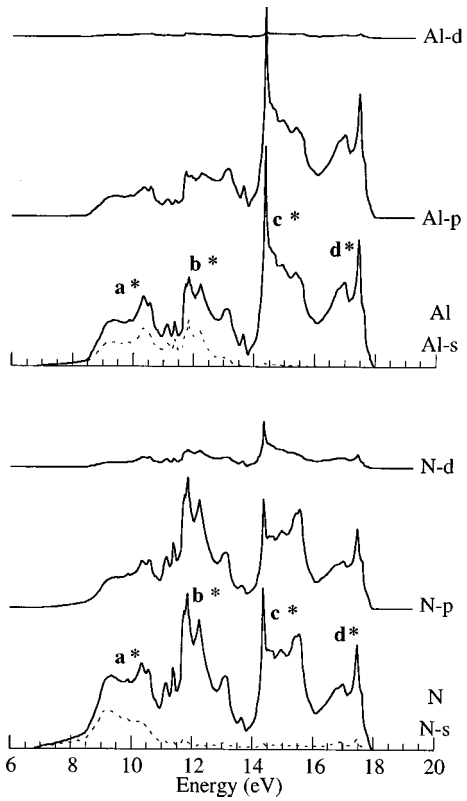

FIG. 8. *s*, *p*, *d* partial density of states for Al and N in AlN deduced from the LMTO method (Ref. 26).

calculations for AlN or by non-self-consistent multiple scattering (MS) calculations for both AlN and AlN(O).

A. Aluminum nitride

The AlN structure consists of a hexagonal arrangement of aluminum atoms, with tetrahedral sites half filled by nitrogen atoms in agreement with the 2-H-wurtzite structure shown in Fig. 6. This structure offers a rather high percentage of free space that can be associated with either tetrahedral or octahedral empty interstitial sites.

1. Density of states calculations

The ground-state electron structures of AlN have been calculated using three self-consistent methods: the augmented spherical wave (ASW) method,[10] the full potential linearized augmented plane wave (FLAPW) method,[11] and the tight-binding linear muffin-tin-orbital method in the atomic spheres approximations (TB-LMTO-ASA or LMTO for short).[12]

All methods are based on density-functional theory (DFT). ASW and FLAPW also employ the local-density approximation (LDA) to account for the effect of exchange and correlation, while in the present stage of LMTO we introduce a generalized gradient approximation description, in which gradient terms of the electron density are added to calculate the exchange-correlation energy.[13]

The ASW method uses the atomic-sphere approximation (ASA), assuming overlapping spheres, centered on the atomic sites, and within which the potential is spherically symmetric. However, the ASA makes the charge density spherical entering the Poisson's equation inside the spheres and neglects the charge outside them. In the present nonclosely packed structure, considering only atom-centered spheres would cause substantial errors. It is therefore necessary to pack the interstitial volume with additional spheres called ''empty spheres.''

In the FLAPW approach, the unit cell is divided into two parts: the nonoverlapping spheres centered on the atomic sites and an interstitial region. Inside the atomic spheres, the basis sets consist of a linear combination of radial functions multiplied by spherical harmonics, while in the interstitial region a plane-wave expansion is used. Even if this method is known to be very accurate, the LMTO basis set orbitals are, on the contrary, more suitable for the chemical interpretation. Consequently, as shown in Fig. 7, which compares total DOS, the FLAPW approach can be considered as a reference for the band-structure calculation. On the other hand, the LMTO method is preferred for the analysis of partial DOS and its results are gathered in Fig. 8. Let us consider the total DOS calculations (Fig. 7). They exhibit a quite striking similarity for the valence-band (VB) occupied states. As for the distribution of unoccupied states corresponding to the conduction band (CB), the band-gap width (5–6 eV) derived from the LMTO calculation, as well as from the FLAPW and ASW calculations, is comparable with the experimental value ($\approx$6.2 eV). Due to the DFT/LDA approach, the energy range above the bottom of the CB accessible with these descriptions remains limited up to about $\approx$12–15 eV. Over this energy range, the CB displays four major peaks at 6.5, 9.5, 12, and 16 eV (this last one being of smaller intensity than the first three) above the top of the VB, even if one notices some slight variations between the details of the unoccupied DOS calculated by the different techniques.

It is well known that high-energy electron-induced transitions obey the general atomic dipole selection rules in the limit of the small-angle scattering, which is the case for our

experimental conditions. Therefore, for an improved comparison with near-edge fine structures visible on core edges, an analysis of the partial density of states projected onto the two different atomic sites (Al and N) and the different *l*-angular momentum (s,p,d) symmetry projections is required. The results obtained from the LMTO calculations are shown in Fig. 8. However, when the atomic site has no center of symmetry in the solid (i.e., tetrahedral), the dipolar condition $(\Delta l = \pm 1)$ is partially relaxed and atomically forbidden transitions become possible.[14]

Over the domain under consideration (≈10–12 eV above the bottom of the conduction band), there is a negligible contribution of the empty Al *d* states, a strong weight of empty *p* states over the three features, and a noticeable weight of empty *s* states for the lowest part. These results generally confirm those obtained in previous studies.[15,16] The first three peaks in the lower parts of the CB have been clearly identified in all cases. The present results confirm that they can be interpreted in terms of the projection of the hybridized *s* and *p* states (N $2p$ states hybridized with Al $3s$ and $3p$ states) on both sites, with a higher proportion of empty *s* states close to the bottom of the CB and empty *p* states at higher energies.

2. MS calculations

An alternative approach is to use the results of MS calculations. One interesting advantage of MS is the ability to isolate the contribution from each atomic shell to the site-specific and symmetry-projected DOS.

MS calculations are based upon the interference between the outgoing spherical wave of the excited electron and the electron wave elastically backscattered from surrounding atoms in a real-space cluster of atoms representing the environment of the atom undergoing excitation. The scattering properties of the various atoms in the cluster are described by phase shifts calculated via solution of the one-electron Schrödinger equation assuming a spherically symmetric muffin tin (MT) form for the crystalline potential.[17,18] MS calculations were performed for both the N *K* and Al L_{23}-ELNES using the ICXANES computer code of Vvedensky, Saldin, and Pendry.[18] Phase shifts (up to $l=3$) and matrix elements were obtained from a non-self-consistent muffin-tin potential calculation on the structure of AlN. A damping term was included to take account of the finite lifetimes of the initial and final states; this was taken to be −0.5, −0.25, and −0.25 eV for the N *K*, Al L_{23}, and Al *K* edges, respectively. The presence of the core hole was accounted for by use of the $(Z+1)^*$ approximation for the central atom in the cluster; inclusion of this effect improves agreement with experimental results for both edges notably in the relative intensity near the edge onset.

For the N *K* edge a full MS calculation as performed for an 8-shell cluster (radius=0.587 nm), whose shell structure may be briefly summarized as follows: shell 1, 4 Al atoms at ~0.19 nm; shell 2, 12 N atoms and 1 Al atom at ~0.31 nm; shell 3, 9 Al atoms at ~0.36 nm; shell 4, 6 N atoms and 6 Al atoms at ~0.44 nm shell 5, 9 Al atoms at ~0.48 nm; shell 6, 2 N atoms at ~0.50 nm; shell 7, 18 N atoms at ~0.54 nm; and shell 8, 12 Al atoms and 12 N atoms at ~0.58 nm. For the Al L_{23} and Al *K* edges an 8-shell cluster of radius 0.587 nm was also employed—the cluster is essentially the same as the nitrogen-based one, except that Al and N atoms are interchanged.

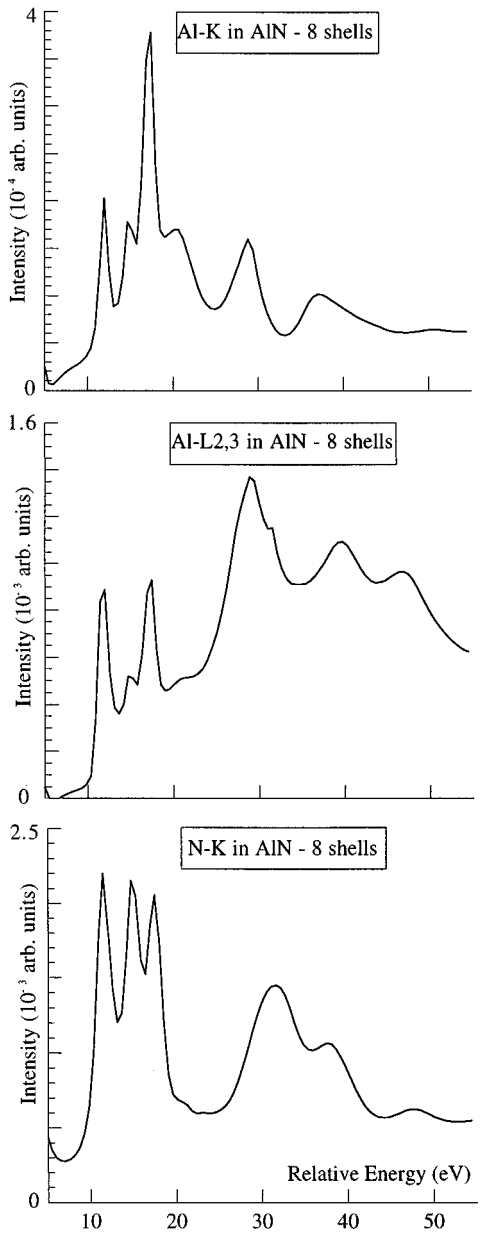

FIG. 9. N *K*, Al L_{23}, and Al *K* ELNES in AlN calculated using multiple scattering theory.

Figure 9 illustrates the results of these calculations that cover a much broader energy range (up to 40 eV above the threshold) than the DOS ones. First, in the N *K*, Al L_{23}, and Al *K* edges, similar 7–8 eV-wide triplet structures are observed. At higher energy, Al L_{23} and N *K* differ slightly in position but much more strongly in intensity. Thus, the Al L_{23} intensity significantly increases, while an inverse phenomenon is observed on the N *K* and Al *K* edges. This clearly demonstrates the importance of *d* states on Al L_{23} at energies typically 20 eV above threshold. These have been well interpreted as due to intra-atomic centrifugal barrier effects.[19]

The contributions from the successive neighboring shells are shown in Fig. 10 for both the N *K* and Al L_{23} edges. In the case of N *K*, the majority of the ELNES is present after

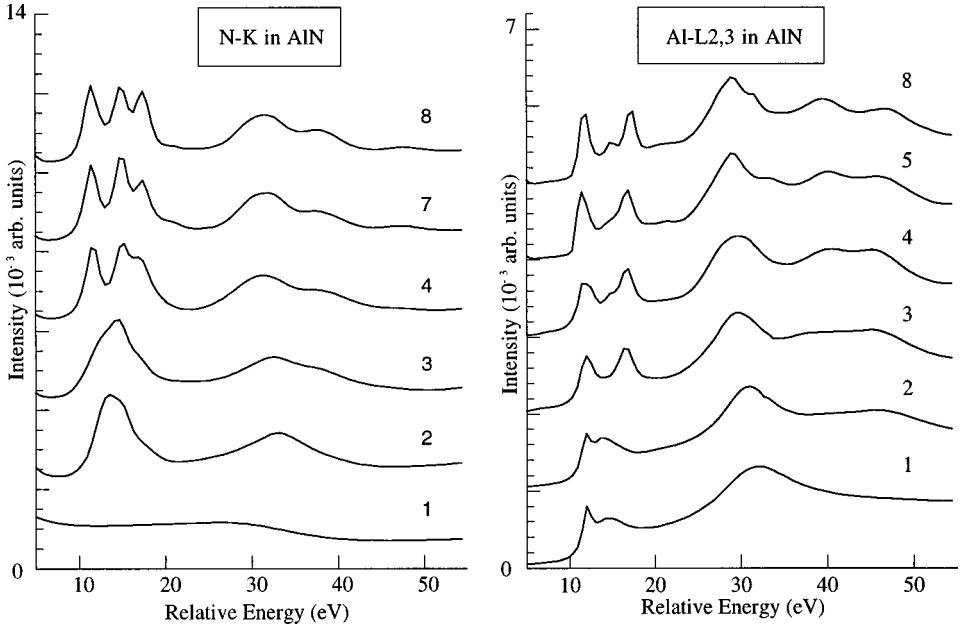

FIG. 10. Effect of increasing number of shells on the calculated N *K* and Al L_{23} edges in AlN.

consideration of four shells, while peaks *d*, and possibly *e*, arise from outerlying shells (shells 7 and 8). In Al L_{23} the second peak, labeled *b*, is only revealed after consideration of eight shells. In both the Al and N edges, nitrogen containing shells exhibit substantially more influence on the ELNES intensity than those containing Al, which confirms the high backscattering strength of electronegative elements such as N.

B. Doped aluminum nitride

In this case, only the MS method can be used because its implementation is more appropriate to the case of complex nonperiodic structures. The different structural models used to simulate the oxygen-doped lattice are based upon the hypotheses suggested from previous EXELFS work,[8] i.e., insertion of oxygen atoms in either tetrahedral sites or octahedral ones. Experimentally, it appears that the N *K* edge is mainly affected by the introduction of O atoms. Therefore, the calculations concern the N *K* fine-structure variations when O is introduced into any of the two types of vacant sites. The corresponding results are shown in Figs. 11 and 12. Strong differences are predicted covering all features from onset up to 40 eV. Most important is the behavior of the lower-energy peak, the intensity of which is moderately reduced in the case of the octahedral insertion. On the contrary, in the tetrahedral insertion, a high and narrow line appears close to threshold, which most likely results from the existence of a very short distance between N and O, transferring most of the low-lying energy states from the nitrogen site to its oxygen nearest neighbors, which are much more electronegative and consequently attract the majority of the VB electrons.

V. DISCUSSION

A. Comparison of experimental and calculated edges in AlN

A general agreement exists between experiment and theory concerning the distribution of accessible final states, with a low-lying triplet of bands covering a total of 7–8 eV and higher accessible states at about 20 eV above threshold. The comparison with MS is in fact excellent in the N *K* and

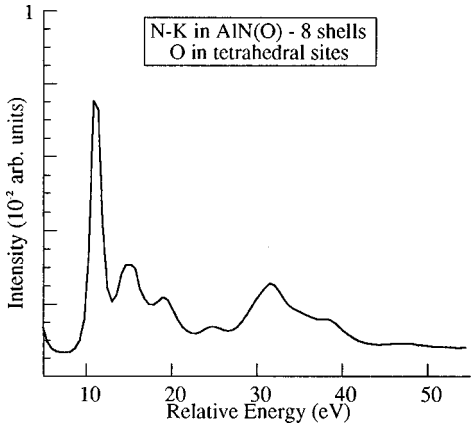

FIG. 11. N *K* edge in O-doped AlN calculated using multiple scattering theory. Oxygen atoms are inserted in the tetrahedral empty sites of the AlN lattice.

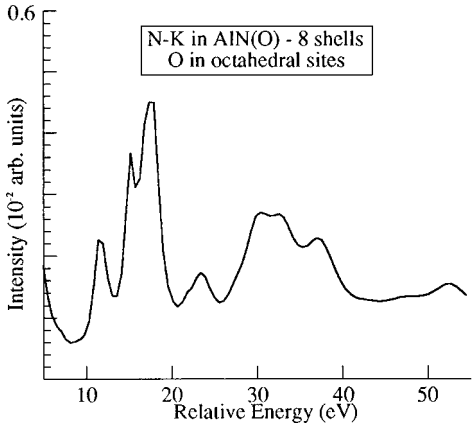

FIG. 12. N *K* edge in O-doped AlN calculated using multiple scattering theory. Oxygen atoms are inserted in octahedral empty sites of the AlN lattice.

Al K cases (see Figs. 2 and 9), where all features appearing over this broad range are well reproduced. This is the reason why we rely mostly on this approach for extending our discussion to the oxygen-doped case. However, there exist some discrepancies in the MS modeling of the Al L_{23} edge, the three peaks are not satisfactorily reproduced and in particular the third peak, which is of lower intensity in experiment, is very high in the calculation. This behavior has not yet been explained. However, some of this discrepancy could be attributed to the existence of transitions to p-like final states in the Al L_{23} edge caused by the breakdown of the spherical symmetry in tetrahedral environments,[14] a situation not adequately modeled by the spherically symmetric MT potential. Consequently, p-like final states have been artificially added to the correctly scaled s- and d-like contributions in the present Al L_{23} MS calculations (Fig. 9) so as to achieve the best agreement with experiment. This approach probably accounts for the observed discrepancies.

For improved understanding of the intensity distribution and variation within the first 12 eV above the threshold, it is therefore useful to compare our measurements for the three edges (Al K, Al L_{23}, and N K) shown in Fig. 2 and the partial DOS calculated in the LMTO model gathered in Fig. 8. The excited $1s$ electrons and the $2p$ electrons from the Al site explore the corresponding densities of final states on Al, with dominant p character in the first case, and (s,d) character in the second one.

If one assumes that the second and the third contributions (b^* and c^*) in the Al-p DOS merge into a single broad peak, one can then directly interpret the intensity profile with the sequence of $a,b+c,d$ peaks on the experimental Al K edge. A similar behavior is observed in the Al K MS results in Fig. 9. On the contrary, the increased weight of peaks a and b, with respect to c and d, at the Al L_{23} edge can be correlated to the stronger a^* and b^* features in the calculated Al s conduction states. As for the nitrogen K edge, the experimental sequence of four peaks (a,b,c,d) is in good agreement with the distribution in intensity within the corresponding peaks labeled a^*,b^*,c^*,d^* in the LMTO calculated N p partial density of states.

In summary, we can identify the low-lying peak of the triplet as being associated with s-like states, and the two higher-lying ones with states of principally p-like character. The higher-lying peak f, which is much more intense in the Al L_{23} edge, is attributed to Al d-like character, as already mentioned. Generally, for all high-energy states lying between 20 and 40 eV above the threshold the observed modulations are well reproduced in the MS simulations, which confirms the validity of this approach in dealing with these features, known as ELNES or XANES oscillations.

B. Mechanisms for oxygen insertion in AlN(O)

1. Center of AlN(O) crystal

Compared to AlN, the N K ELNES from the central part of the AlON dendrite exhibits a reduction in the first peak intensity, while the corresponding Al L_{23} ELNES does not show any significant differences. Consideration of the MS calculations for the N K edge in model AlN(O) clusters in Fig. 11 suggests that the reduced first peak intensity should be associated to the insertion of oxygen atoms in one of the empty octahedral sites within the AlN unit cell. This is an initial simple explanation.

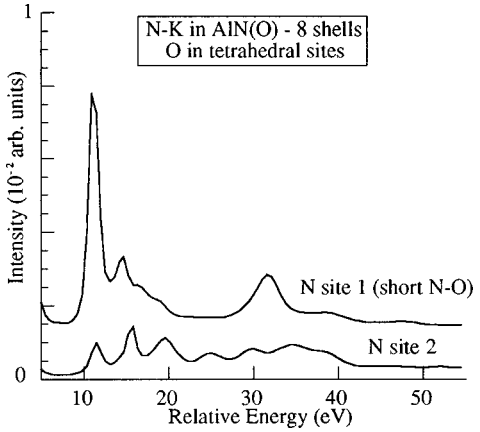

FIG. 13. N K edge MS calculation for O inserted in tetrahedral sites in AlN for the two unequivalent N atomic sites.

However, an alternative explanation cannot be ignored when considering that HREM (high resolution electron microscopy) studies have demonstrated the presence of stacking faults in the center of the dendrite.[20] These stacking faults involve lateral displacement of the tetrahedral sites, so that the insertion of an O atom in one of these empty tetrahedral sites can be accommodated without the existence of a short N-O distance.[21] These findings have led us to reconsider more explicitly our MS calculations for the tetrahedral insertion case.

Incorporation of oxygen in only one of the vacant tetrahedral sites in the AlN unit cell leads to the presence of two unequivalent N sites, one of which has a very short N-O distance (where adjacent tetrahedra share faces), while the other site exhibits a significantly longer distance (where adjacent tetrahedra share only one edge).[21] The decomposed MS results for these two N sites (Fig. 13) show that the short N-O distance clearly gives rise to the strong intensity of the first peak in the N K ELNES. From the chemical viewpoint this may be understood as arising from the emptying of electronic states close to the Fermi level in the local nitrogen DOS due to the close approach of a more electronegative oxygen atom. However, the site with the long N-O distance exhibits a reduction in intensity of the first peak, which could also correspond to our observations (Fig. 4) if we assumed that oxygen incorporation is associated with stacking faults in the central part of the dendrite as has been observed at inversion domain boundaries (IDB's) in sintered oxygen-doped AlN pellets.[22] It is interesting to note that the N K ELNES observed at IDB's also appears to possess a reduced intensity of the first peak.[22]

2. Outer part of AlN(O) crystal

Our previous EXELFS analysis[8] on the outer part of the crystals demonstrated that the insertion of oxygen would preferentially involve octahedral sites. This is in contradiction with our present experiments, where the origin of the strong line on the N K threshold should be attributed to oxygen insertion in a tetrahedral site from the results of our MS simulations. However, we believe that this cannot be the

correct explanation for several reasons. First, the O *K*-edge peak does not exhibit correlated strong changes spectra from the two parts of the specimen. This is more surprising as there is an increase in oxygen content in these areas, up to a level of doping still sufficiently low to prevent substitution of N by O from occurring.

As a matter of fact, we attribute the observed profile for the N *K* edge to strongly enhanced radiation damage induced by the primary electron beam, this effect being more intense with the high current doses (of the order of $10^9-10^{10}e/\mathrm{nm}^2$ involved) in the probe of the FEG-STEM. Measurements of the dose dependent edge decay on a specimen with a higher oxygen-doping level have indicated the removal of oxygen and an increase in the absolute level of nitrogen during irradiation (Fig. 5). This was associated with an abrupt increase in the relative intensity of the first peak in the N *K* ELNES. A similar behavior has been observed in first-peak intensity of the N *K* ELNES obtained from the outer part of the dendrites.

Therefore, the curve drawn in dotted lines in Fig. 4 shows the corresponding spectrum of the N *K* ELNES from the outer part of the dendrite measured with a less intense probe (of dimension 10 nm) in a CM30 Philips TEM fitted with a LaB_6 filament and a Gatan 666 PEELS, giving an overall spectral energy resolution of 1.2 eV. This spectrum is less sensitive to the dose and shows a slightly reduced first-peak intensity as compared with the N *K* ELNES of AlN. In this area, we can therefore conclude that our results confirm the general insertion of oxygen atoms in the octahedral sites. Note that there are no stacking faults visible in the HREM images of this external region, which could provide ''relaxed'' tetrahedral vacancies. The presence of an intense narrow line at threshold only reveals the strong influence of radiation damage and could be attributed to the local trapping of gaseous N_2 whose intense π^* peak lies at 400 eV.[23]

VI. CONCLUSION

Electron energy-loss spectroscopy has been shown to constitute a powerful tool for the local investigation of electronic states in aluminum nitride, either pure or doped with oxygen atoms. The interpretation of the observed spectral features requires strong efforts in modeling the distribution of unoccupied states in the conduction band. The projected DOS curves provide a good support for understanding the nature of the lower-lying states, up to about 12 eV above threshold, while the multiple scattering approach is also very well adapted for dealing with the observed oscillations in the $\approx$20–50-eV range. The analysis of the nature of the preferential sites for oxygen doping, in the center as well as in the outer part of the dendrites, seems to confirm the preferential insertion of oxygen in octahedral sites despite the possible influence due to the presence of stacking faults in the central part of the dendrite and the occurrence of increased beam sensitivity in the outer part of the dendrite.

[1] E. Ruiz, S. Alvarez, and P. Alemany, Phys. Rev. B **49**, 7115 (1994).

[2] G. Partridge, Adv. Mater. **4**, 51 (1992).

[3] D. G. Böcker, R. W. Hamminger, J. Heinrich, J. Huber, and A. Roosen, Adv. Mater. **4**, 169 (1992).

[4] G. A. Slack, R. A. Tanzilli, R. O. Pohl, and J. W. Vandersande, J. Phys. Chem. Solids **48**, 641 (1987).

[5] B. Aspar, R. Rodriguez-Clemente, A. Figueras, B. Armas, and C. Combescure, J. Cryst. Growth **129**, 56 (1993).

[6] C. Colliex, M. Tencé, E. Lefevre, C. Mory, H. Hu, D. Bouchet, and C. Jeanguillaume, Mikrochim. Acta **71**, 114 (1994).

[7] M. Tencé, M. Quartuccio, and C. Colliex, Ultramicroscopy **42**, 58 (1995).

[8] S. Abaidia, V. Serin, G. Zanchi, Y. Kihn, and J. Sevely, Philos. Mag. A **72**, 1657 (1995).

[9] A. J. Craven, J. Microsc. **180**, 250 (1995).

[10] M. Williams, P. Kübler, and R. Gelatt, Phys. Rev. B **19**, 6094 (1979).

[11] P. Blaha, K. Schwartz, P. Sorantin, and B. Trickey, Comput. Phys. Commun. **59**, 399 (1990).

[12] O. K. Andersen, Phys. Rev. B **12**, 3060 (1975); O. K. Andersen and O. Jepsen, Phys. Rev. Lett. **56**, 2571 (1984); O. K. Andersen, O. Jepsen, and D. Glötzel, in *Highlights of Condensed-matter Theory*, edited by F. Bassani and F. Fumi (North Holland, New York, 1985); W. R. L. Lambrecht and O. K. Andersen, Phys. Rev. B **34**, 2439 (1986).

[13] J. P. Perdew, Phys. Rev. B **33**, 8822 (1986).

[14] P. L. Hansen, R. Brydson, and D. W. McComb, Microsc. Microanal. Microstruct. **3**, 213 (1992).

[15] S. Loughin, R. H. French, W. Y. Ching, Y. N. Xu, and G. A. Slack, Appl. Phys. Lett. **63**, 1182 (1993).

[16] W. Y. Ching and B. N. Harmon, Phys. Rev. B **34**, 5305 (1986).

[17] L. F. Mattheiss, Phys. Rev. **133**, A1399 (1994).

[18] D. D. Vvedensky, D. K. Saldin, and J. B. Pendry, Comput. Phys. Commun. **40**, 421 (1986).

[19] C. Colliex, in *Advances in Optical and Electron Microscopy*, edited by R. Barer and V. E. Cosslett (Academic, New York, 1984), p. 110.

[20] D. Dorignac, A. Mazel, Y. Kihn, and J. Sevely, J. Eur. Ceram. Soc. **13**, 345 (1994).

[21] G. Van Tendeloo, K. T. Faber, and G. Thomas, J. Mater. Sci. **18**, 525 (1983).

[22] J. Bruley, A. D. Westwood, R. A. Youngman, J. C. Zhao, and M. R. Notis, in *Structure and Properties of Interfaces in Ceramics*, edited by D. A. Bonnell, U. Chowdhry, and M. Ruhle, MRS Symposia Proceedings No. 357 (Materials Research Society, Pittsburgh, 1995), p. 265.

[23] A. P. Hitchcock, Phys. Scr. **T31**, 159 (1990).

[24] FLAPW and ASW have been carried out for 784 *k* points in the irreducible wedges of the first Brillouin zone of the hexagonal lattice. Within the ASA the nonunique choice of the AS radii was subjected to interatomic distances. The following radii: $r(\mathrm{Al})=1.13r(\mathrm{ES})$ and $r(\mathrm{N})=1.44r(\mathrm{ES})$ have been found to minimize the overlap between the AS.

[25] Atomic spheres radii and positions: Al, 1.196 Å; N, 0.988 Å; $E1$ (0, 0, 0.2257), 1.161 Å; $E2$ (2/3, 1/3, 0.1749), 0.693 Å; $E3$ (1/8, 1/4, 0.4849), 0.427 Å; $E4$ (0, 1/2, 0.2222), 0.383 Å. The full LMTO basis set consisted of the $3s$, $3p$, and $3d$ functions for

the Al spheres, of the $2s$, $2p$, and $3d$ functions for the N spheres, and s, p, and d functions for the empty spheres. The optimum number of empty spheres and atomic-sphere radii was found comparing the total DOS from FLAPW and LMTO and using the extended basis set given above. The **k**-space integration was performed with the tetrahedron method and the charge self-consistency and average properties was obtained from 152 irreducible **k** points.

[26] For the orbital analysis using the projected DOS, a smaller and more realistic basis set was used. All the empty sphere LMTO's were downfolded (see Ref. 8 for more details) and only the Al and N s and p LMTO's were kept for the eigenvalue problem.